# Femtosecond versus nanosecond laser micro-machining of InP – a nondestructive three-dimensional analysis of strain

Lu Xu [(1)], Donnacha Lowney[(1)], Patrick J McNally[(1)], A. Borowiec[(2)], H. K. Haugen[(2)], A. Lankinen[(3)], T. O. Tuomi[(3)], A. N. Danilewsky[(4)]

1) School of Electronic Engineering, Dublin City University, D9, Dublin, Ireland
2) Department of Engineering Physics, McMaster University, Hamilton, Ontario, Canada L8S 4M1
3) Optoelectronics Laboratory, Helsinki University of Technology, P.O. Box 3500, FIN-02015 TKK, Finland
4) Kristallographisches Institut, University of Freiburg, D-79104 Freiburg, Germany

## 1. Abstract:

Ultra-fast femtosecond laser micro-machining can lead to improved surface morphology and a reduction in the heat-affected zone. In this paper, synchrotron x ray topography (SXRT) and micro-Raman (μRS) has been used as nondestructive tools to compare the residual strain in InP substrates after femtosecond and nanosecond laser processing. 2-dimensional stain distributions with varying probing depth and cross section images across the 4 laser machined grooves were obtained. The re-crystallized poly-InP layer on the laser machined groove surface has been found to be highly strained in tension and the stress magnitude is much bigger than the shear stress introduced by crystal distortion underneath. After comparing the simulation results of SXRT orientation contrast with the topography images, the nature of the crystal plane distortion induced by both fs and ns laser machining methods was elucidated.

**Keywords:** Femtosecond laser ablation; Indium phosphide; Raman spectroscopy; Synchrotron x-ray topography; Strain analysis

## 2. Introduction

Indium phosphide (InP) has been found to be one of the promising Ⅲ-Ⅴ compound semiconductor materials for high speed optoelectronic applications and this has drawn great attention in the past few years. Compared with conventional nanosecond (ns) laser methods, ultra-fast femtosecond (fs) laser pulses are particularly advantageous in high precision laser ablation, which can lead to improved surface morphology and a reduction in the extent of the heat-affected zone (HAZ). The quality difference of machined substrates with different laser pulse durations, in terms of collateral damage of the crystal structure, residual strain and

localized change in optical, mechanical and electronic properties, has been demonstrated by many groups.

Typically, the non-destructive studies on laser machined samples have been limited to the top surface using optical (OM), scanning electron (SEM) [1] and atomic force microscopy (AFM) for surface morphology visualization [2], micro-Raman spectroscopy (μRS) for stress analysis [2,3] and Auger electron spectroscopy (AES) for chemical modification [4]. Thus, according to most of the published work, in order to obtain the crystal structure and strain information tens of microns under the laser machined surface, the samples have to be destructively cleaved or further prepared by some special techniques e.g. focused iron beam (FIB) to allow access to the cross-sectional facet by the degree of polarization (DOP) photoluminescence (PL) techniques [5] and transmission electron spectroscopy (TEM) [6].

Since the threshold fluence dependency of irradiated semiconductors on the number of laser pulses can be described by a fatigue damage mechanism, it becomes very important to understand the accumulated mechanical stress in the multiple-pulse laser machining process. [7] This stress can be induced by the thermal process, top surface chemical compositional changes and the crystal structure distortion underneath.

In this paper, we present a totally non-destructive 3D analysis of strain induced by femtosecond and nanosecond laser machining using white beam synchrotron x-ray topography (SXRT) and high resolution micro-Raman Spectroscopy (μRS). 2D images with varying probing depth and cross section images of the strain fields right through the processed InP wafer have been obtained. Both uniaxial and shear stress values from the top surface and the underlying crystal have been calculated based on the Raman peak shifts and the orientation contrast of SXRT images. To the best of our knowledge, it is the first time that white beam synchrotron x-ray topography (SXRT) has been applied to the strain analysis of laser machined samples.

The method of strain field imaging using SXRT is based on two contrast mechanisms: (1) extinction contrast: the difference in reflecting power between perfect and imperfect crystal regions and (2) orientation contrast: the non-uniform diffracted image of distorted crystal whose misorientation exceeds the divergence of the synchrotron beam, ~0.06 mrad vertically in this study. The SXRT sensitivity to strain magnitude is estimated to be at least of the order of $6\times10^{-5}$ and a spatial resolution of about 5μm can be easily achieved [8]. Unlike the aforementioned strain characterization techniques used on laser machined samples, SXRT is a genuinely nondestructive analysis tool sensitive to the subsurface features. By selecting different diffraction images on the recording film and varying the corresponding X-ray penetration depth, a 3D strain field profile right through from the top-side to back-side can be built up. Using transmission section topography (TS) geometry, a set of

cross-section images of the strain distribution on different crystal planes can be obtained in a few minutes. SXRT has already been successfully used to characterize the defects in single crystal Si, thermal processing induced strain fields in packaged Si integrated circuits and solder bump process induced stress distributions in Si substrates [9-11].

One drawback to be noted at this stage is that it is normally very difficult to determine the sign of the strain which produced the contrast on the recording film and only the magnitude of the strain can be calculated based on SXRT results. Therefore, in order to calculate the exact stress value, obtain a high resolution stress line profile (less than 1 μm spatial resolution) and also analyze the crystalline structural modification on the top surface, micro-Raman Spectroscopy (μRS) has also been used as a complementary tool in this study.

## 3. Experimental details

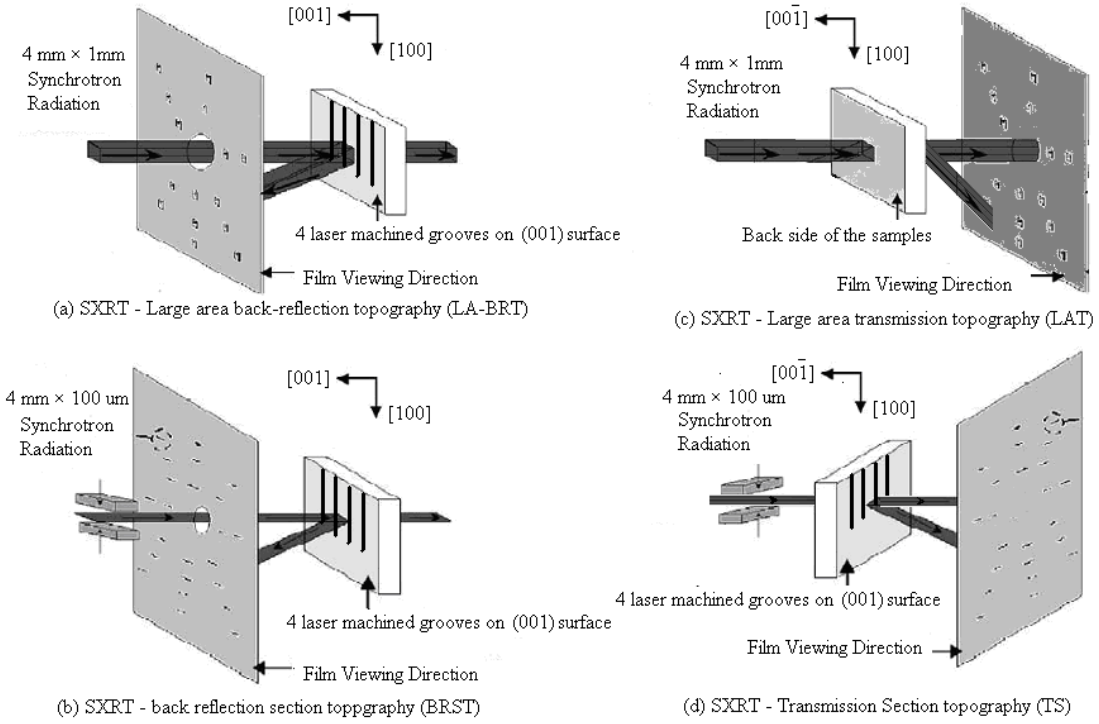


**Figure 1.** (a) Schematic details of large area back-reflection topography (LA-BRT) geometry, (b) back-reflection section topography (BRST) geometry, (c) large area transmission topography (LAT) geometry and (d) transmission section topography (TS) geometry

The micro-machined samples are prepared with a commercial, regeneratively amplified Ti:sapphire laser operating at a centre wavelength of 800 nm at a 1 kHz

repetition rate. The laser beam was focused on the sample surface by a 5× microscope objective to a spot size of 5.5±0.5 μm (Gaussian beam radius at $1/e^2$ intensity fall off). Inside a small vacuum chamber, four grooves were machined on the (001) surface of one n-InP substrate (S doped ~$10^{18}$ $cm^{-3}$) along the [100] direction under a rough vacuum of 0.1 Mbar. The pulse durations are approximately 130 femtoseconds and 8 nanoseconds. The nanosecond pulse is obtained from the same laser as the 130 fs pulse by blocking the seed pulse to the amplifier and bypassing the compressor. With a beam linearly polarized perpendicular to the cutting direction, pulse energies of 1.0 μJ (fluence of ~ 2 J/$cm^2$) and 0.35 μJ (fluence of ~ 0.7 J/$cm^2$) were utilized at a machining rate of 500 μm/s, as shown in table 1. This machining rate implies approx. 10 pulses are incident on the sample in each beam diameter length, making this a multi-pulse process.

The X-ray topography measurements were performed at HASYLAB-DESY, Hamburg, Germany, utilizing the continuous spectrum of synchrotron radiation from the DORIS III storage ring bending magnet source. The ring operated at a positron energy of 4.45 GeV and at typical currents of 80–150 mA. The Laue patterns of topographs were recorded on Geola VRP-M Holographic films, which has an emulsion grain size of about 40 nm. Four experimental arrangements, large area back-reflection topography (LA-BRT), back-reflection section topography (BRST), large area transmission topography (LAT) and transmission section topography (TS), as illustrated in Figure 1, have been used to obtain depth profile information and cross-section images of the strain fields.

Micro-Raman measurements were conducted in the backscattering geometry using a 488 nm $Ar^+$ laser (13.2mW) excitation at room temperature on a Jobin Yvon LabRam HR800 μRS system equipped with a liquid nitrogen cooled CCD detector (wavenumber resolution = 0.4 $cm^{-1}$). With an Olympus 100× microscope objective, the laser was focused on the sample surface to a diameter of 1 μm. Line scanning with 1 μm step size was performed automatically on a motorized XY microscope stage whose step resolution is 0.1 μm and reproducibility is 1 μm. 20 seconds integration time was selected and 3 Raman spectra from the same probing position were averaged to increase the signal to noise ratio (SNR).

## 4. Results and discussion

### SXRT Large area back reflection (LABRT) results

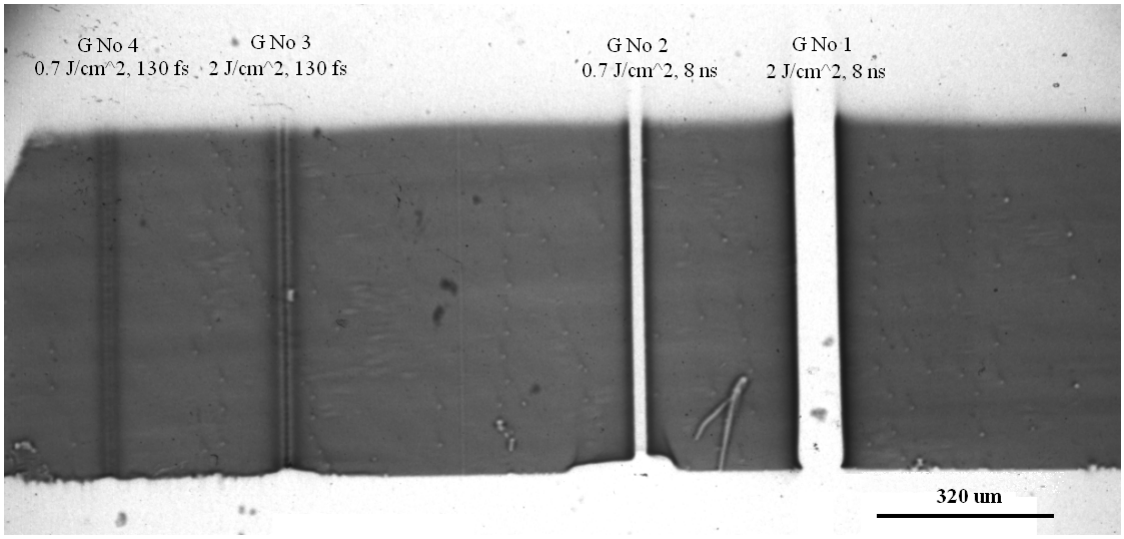


**Figure 2:** Typical SXRT LA-BRT images for 4 laser machined grooves: 0 2 6 diffraction image. The diffraction vector **g** is indicated on the image.

As shown in figure 2, the 0 2 6 large area back-reflection topograph (LA-BRT), two nanosecond laser machined grooves (G No1 and G No 2) can be observed as two strips of reduced intensity (white) at the grooves' center and enhanced x-ray diffraction intensity (black) at the edges. In contrast, the two femtosecond laser machined grooves (G No3 and G No 4) appear to have increased diffraction intensity at their respective centres.

The kinematic penetration depth ($t_p$) of the x-rays in each SXRT diffraction image, which is measured perpendicular to the surface, can be calculated using the equation:

$$t_p = \frac{1}{\mu\left(\frac{1}{\sin(\alpha_i)} + \frac{1}{\sin(\alpha_f)}\right)} \quad (1)$$

where $\mu(\lambda)$ is the linear x-ray absorption coefficient at wavelength $\lambda$, $\alpha_i$ and $\alpha_f$ are the incidence and exit angles with respect to the sample surface [12]. Therefore, the probing depth of the 0 2 6 diffraction image can be estimated to be 2.78 μm, which is far deeper than the probing depth of the Raman measurement (~70 nm with 488 nm laser excitation).

Two possible mechanisms can be used to explain the intensity contrast at the groove centres for all four laser machined grooves shown in figure 2. The extinction contrast mechanism suggests that the reduced intensity around the grooves may represent the greatly reduced x-ray diffractive capability due to the presence of a thick x-ray absorbing re-solidified surface layer, which comprises a high percentage of amorphous or polycrystalline InP. However, the cross sectioned transmission electron microscope (XTEM) results for the same sample presented by another group [6]

indicates that the resolidified layer thickness only varies from 200 nm to 500 nm, which is far less than the x-ray penetration depth calculated using equation 1. Additionally, the width of the white low x-ray intensity region is much bigger than the groove width or the re-solidified layer width across the grooves (from 10 μm to 20 μm measured by XTEM). Therefore, this image can only be explained by a dominant orientation contrast mechanism, resulting from the overlap or separation of an inhomogeneously diffracted x-ray beam.

The width of the reduced intensity stripes on the SXRT film should be equal to the SXRT detectable width of shear strained InP crystal 2.78 μm below the top surface. Therefore, according to figure 2, the width of the distorted underlying crystal near the four grooves from No.1 to No.4 can be estimated to be 64 μm, 32 μm, 28 μm and 24 μm respectively, as listed in table 2. With the same laser pulse energy, laser machining with shorter pulse duration leads to smaller strained regions near the grooves.

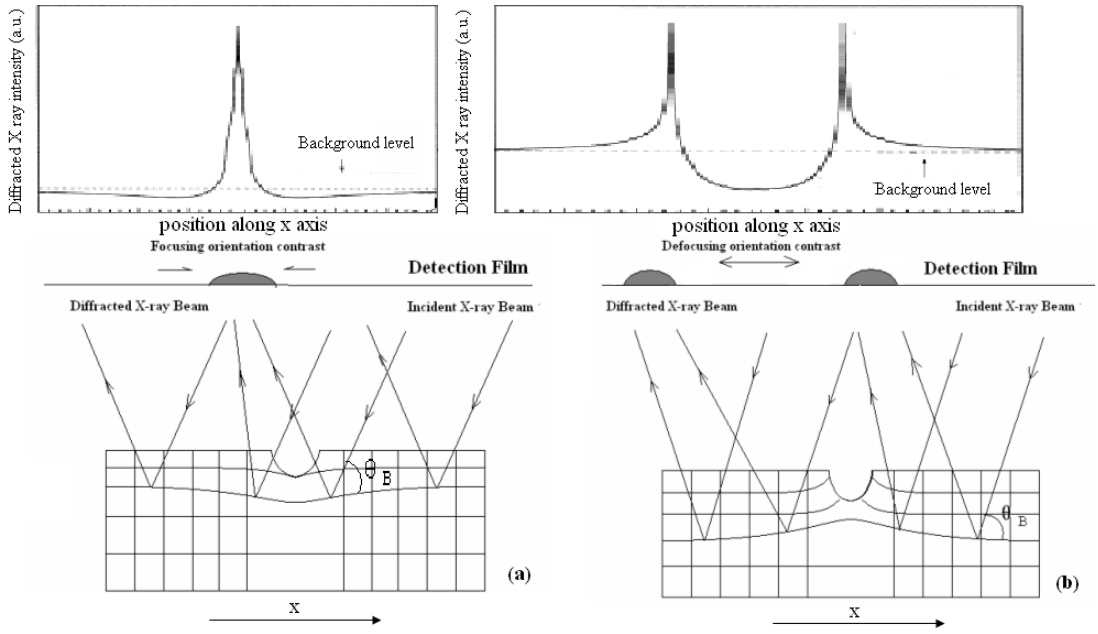


**Figure 3:** Schematic of 'focusing' (a) and 'defocusing' (b) mechanism of diffraction x-ray intensity line profile with two oppositely shear strained areas associated with femtosecond and nanosecond laser machining respectively.

In addition, two totally different diffracted x-ray line profiles, termed here as 'focusing' and 'defocusing' phenomena, are observed across the fs and ns laser machined grooves respectively. Similar to SXRT orientation contrast for edge dislocations [13], these phenomena can be explained by the opposite sign of (0 0 1) crystal plane Bragg angle variation ($\Delta\theta_B$) with respect to the incident direction of

synchrotron x-ray beam in the shear strained area. Referring to figure 3(a), the femtosecond laser machining process modified the subsurface (0 0 1) crystal plane such that the diffracted x-ray intensity from the distorted region is ‘focused’ to the groove center, shown as a symmetric white-black-white sandwich structure contrast in the LA-BRT image. In contrast, for the nanosecond laser machined trenches, as shown in figure 3(b), the diffracted x-rays from the shear strained area is ‘defocused’ to the groove sides, resulting in a wide white stripe structure with enhanced intensity at the edges along the [1 0 0] direction. According to the ‘defocusing’ orientation contrast observed, the subsurface (0 0 1) crystal planes tilt upwards and tend to align perpendicularly to the laser machined surface when approaching the groove centre. One possible reason could be that during the time between two nanosecond laser pulses, which is longer than the time need for thermal diffusion deep into the bulk, a heat affected zone (HAZ) is built up by the excess heat induced by the initial laser pulse. The (0 0 1) crystal planes in the HAZ are deformed along the temperature gradient, which is normal to the laser machined surface. A tensile strained area could be expected in the underlying crystal substrate after the nanosecond laser machining process. In contrast, the (0 0 1) crystal planes under the femtosecond laser machined grooves are simply compressed downwards and leave a compressively strained area below the groove center, as shown in Figure 3(a). In this case, non-thermal melting occurs. Similar imaging results of shear strain distribution have been observed using a destructive probing method (degree of polarization photoluminescence technique) on the cleaved InP facet across all four laser machined grooves, where the degree of polarization (DOP) signal, associated with linear strain, and the rotated degree of polarization (ROP) signal distribution, which is directly related to the shear strain and lattice distortion direction, have been found to be of opposite sign beneath the fs and ns laser machined grooves [5]. Although the extinction contrast mechanism may have some minor impact on the LA-BRT images especially for the fs laser machined case where dislocations along groove sides and twins at the center are observed by XTEM [6], the dominant orientation contrast mechanism still clearly indicates the opposite sign of crystal distortion in the two cases. This conclusion is further confirmed by the SXRT transmission section topography (TS) simulations in section 4.3.

**SXRT back reflection section topography (BRST) results**

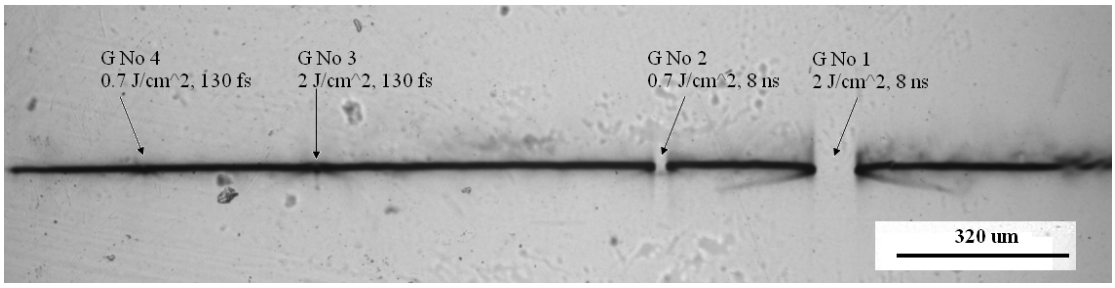


**Figure 4:** The 0 2 6 SXRT back reflection section topography (BRST) of four laser machined grooves with x-ray penetration depth ($t_p$) of 2.8 μm.

One of the advantages of SXRT back reflection section topography is its ability to provide nondestructive depth profiling of a thin slice of InP crystal across the 4 laser machined grooves perpendicular to the top surface. By carefully comparing the topographs and the corresponding x-ray penetration depths for different diffracted images, the depth of imperfect crystal region can be estimated. As shown in figure 4, the broken line features (defocusing orientation contrast) introduced by nanosecond laser machining process can be found on this BRST image with $t_p$=2.8 μm and all the other diffracted images on the recording film. The corresponding x-ray penetration depth varies from 1.5 μm for 1 1 5 diffraction to 22.5 μm for 3 3 13 diffraction. Therefore, the magnitude of shear strained depth induced by nanosecond laser machining is greater than 20 μm. At the positions of G No.3 and G No.4 in figure 4, the SXRT misorientation contrast of trifurcate shape related to the distorted InP crystal under femtosecond laser machined grooves is not obvious, which indicates much smaller shear strain values about the fs machined grooves compared to the nanosecond processed counterparts. Among all the studied diffraction images, the strongest SXRT misorientation contrast about G No.3 and G No.4 can be found in the 0 2 6 diffraction, which suggests that the most imperfect crystal region induced by fs laser machining is about 3 um below the top surface.

**Transmission section results and simulation**

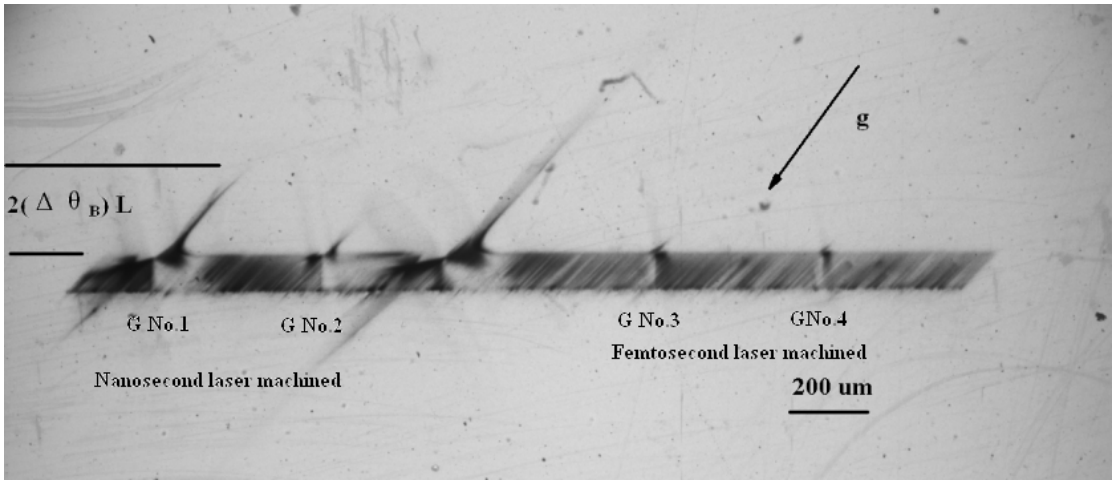


**Figure 5**: The $\bar{2}\,\bar{2}\,0$ SXRT Transmission Section Image of laser machined InP

As shown in figure 5, the $\bar{2}\,\bar{2}\,0$ SXRT transmission section (TS) image, four pairs of symmetric back 'tails' can be observed around all laser machined grooves. This contrast can been seen when the misorientation of crystal planes exceeds the synchrotron x-ray beam divergence, which is 0.06mrad vertically at the F1 beamline in HASYLAB. The black tail length, corresponding to the magnitude of orientation contrast shift ($\Delta S$), can be calculated as [14]:

$$\Delta S = 2\ (\Delta\theta_B)\ L \tag{2}$$

where $\Delta\theta_B$ is the maximum observed shift of the Bragg angle of the severely strained crystal region and L is the distance between the sample and film (93 mm in this case). $\Delta\theta_B$ comprises lattice dilatation ($\Delta d/d$) parallel to the Burgers vector (**g**) and the component of the tilt angle α of the lattice planes around [0 1 0], the normal to the plane of X-ray incidence, and this can be expressed as [14]:

$$\Delta\theta_B = \frac{\Delta d}{d}\ \tan\ (\theta_B) + \alpha \tag{3}$$

Since white beam radiation can provide a diffracting wavelength for any dilated plane, the dilatation components $(\Delta d/d)\tan\theta_B$ can be ignored and $\Delta\theta_B$ is equal to tilted angle α, which is directly related to the shear strain $\gamma_{xy}$ [15].

$$\gamma_{xy} \approx \Delta\theta_B \approx \alpha \tag{4}$$

The magnitude of shear stress ($\delta_{xy}$) can been quantitatively estimated using

$$| \sigma_{xY} | = E | \gamma_{xY} | \quad (5)$$

where E = 61.1GPa, the Young's modulus of InP [16].

Using the orientation contrast shift ($\Delta S$) measured in figure 5 and equations (2) and (3), the maximum distorted angle of the $(\bar{2}\,\bar{2}\,0)$ lattice plane about the laser machined grooves from No.1 to No.4 has been estimated to be 1.74 mrad, 0.54 mrad, 0.35 mrad and 0.24 mrad, respectively. The magnitude of crystal misorientation resulting from femtosecond laser machining is far less than the comparable nanosecond process with the same laser pulse energy. With reduced peak laser fluence from 2 J/cm$^2$ to 0.7 J/cm$^2$, the shear stress value about the grooves decreases from 106.2 MPa to 33.4 MPa for the nanosecond laser process and from 22.2 MPa to 14.1 MPa for the femtosecond processes, as listed in table 1.

Additionally, as shown in figure 5, the orientation contrast induced black tail, which extends upwards on the right hand side of the nanosecond laser machined grooves at positions G No.1 and 2, extends downwards on the same side of femtosecond grooves at positions G No.3 and 4. It confirms that the region where the crystal planes are downward misoriented for the femtosecond laser machined samples become upward misoriented for the nanosecond machined samples and vice versa, as illustrated by figures 3(a) and 3(b) respectively.

To further confirm the opposite sign of the distorted crystal planes underneath the machined grooves, two typical SXRT TS images are simulated for grooves No.3 and No.1 with Matlab® using the methods of [17] for the orientation contrast mechanism. The simulation is based on the parameters calculated above, such as the strained region width and the maximum distorted angle of the $(\bar{2}\,\bar{2}\,0)$ lattice planes. The bending directions for both fs and ns cases are assumed to be the same as the predictions shown in figure 3. To simplify the simulation, only a single distorted (0 0 1) crystal plane several micrometers below the surface has been considered. The distorted crystal planes on either side of the laser machined grooves are separated by the groove width of 4 μm. As shown in figure 6(a) and (b), the (0 0 1) plane misorientation magnitude $\Delta\theta_B$ is assumed to increase more and more rapidly when approaching the grooves' centre and is arbitrarily described by a function of distance y measured from the centre of the grooves:

For the nanosecond laser machined groove #1:

$$\Delta\theta_B(y) = 0 \quad \text{when } |y|>34 \text{ or } |y|<2$$

$$\Delta\theta_B(y) = -\Delta\theta_{B_{max}}\left(1-\sqrt{\cos\left(\frac{34-|y|}{64}\right)\pi}\right) \quad \text{when } 2<|y|<34 \qquad (6)$$

For the femtosecond laser machined groove #3:

$$\Delta\theta_B(y) = 0 \quad \text{when } |y|>16 \text{ or } |y|<2$$

$$\Delta\theta_B(y) = \Delta\theta_{B_{max}}\left(1-\sqrt{\cos\left(\frac{16-|y|}{28}\right)\pi}\right) \quad \text{when } 2<|y|<16 \qquad (7)$$

where the positive value of $\Delta\theta_B$ represents the clockwise rotation along the [100] direction and the y axis is defined along the [010] direction.

This simulation method is based on orientation contrast purely and can be applied to any diffraction images observed on the detection film. Briefly, a set of crystal planes (h k l), which give the h k l diffraction image on the recording film, are represented by plane normal **B** and distorted around the [100] axis **A** by $\Delta\theta_B(y)$. The resulting vector **C** can be calculated as:

$$\vec{C} = \vec{B_A} + \vec{A}\times\left(\vec{B}-\vec{B_A}\right)\frac{\sin(\Delta\theta_B(y))}{A} + \cos(\Delta\theta_B(y))\left(\vec{B}-\vec{B_A}\right) \qquad (8)$$

where
$$\vec{B_A} = \frac{\vec{A}\cdot\vec{B}}{A^2}\vec{A} \qquad (9)$$

Due to the SXRT TS experimental setup, the whole crystal is then rotated around the [010] axis **D** by 13°to image reflections of interest. The distorted crystal plane [h k l] is therefore rotated to a new direction **E** [$h_r$ $k_r$ $l_r$] to reflect the incident synchrotron x ray beam along the [0 0 1] direction.

$$\vec{E} = \vec{C_D} + \vec{D}\times\left(\vec{C}-\vec{C_D}\right)\frac{\sin(13^\circ)}{D} + \cos(13^\circ)\left(\vec{C}-\vec{C_D}\right) \qquad (10)$$

where
$$\vec{C_D} = \frac{\vec{C}\cdot\vec{D}}{D^2}\vec{D} \qquad (11)$$

The angle$\theta_{r,[001]}$ between the incident synchrotron x-ray beam [0 0 1] and the reflecting crystal plane normal **E** [$h_r$ $k_r$ $l_r$] is

$$\theta_{r,[001]} = \arccos\left(\frac{l_r}{\sqrt{h_r^2+k_r^2+l_r^2}}\right) \qquad (12)$$

The distance r between the reflected spot and the film centre for the SXRT transmission section experimental set up can be calculated as

$$r = L\tan(2\theta_{r,[001]}-\pi) \qquad (13)$$

where L is the distance between sample and film (93 mm in this study).

Since the distorted reflecting crystal plane normal **E** [$h_r$ $k_r$ $l_r$], incident x-ray beam [001] and reflected x-ray beam should be inside the same plane, the coordinates $x_r$ and $y_r$ of the simulation point on the film are:

$$\mathbf{x_r} = \frac{\mathbf{h_r}}{\sqrt{\mathbf{h_r}^2 + \mathbf{k_r}^2}}\,\mathbf{r}$$
$$\mathbf{y_r} = \frac{\mathbf{k_r}}{\sqrt{\mathbf{h_r}^2 + \mathbf{k_r}^2}}\,\mathbf{r} \qquad (14)$$

where $x_r$ is along the [100] direction and $y_r$ is along the [010] direction.

Since $\Delta\theta_B$ is a function of the initial reflecting point position (y) on the InP sample, a set of coordinates for the final reflected points' positions on the film can be calculated and a simulated transmission section image originating from a single layer of the distorted crystal plane can be plotted, as shown in figure 6(c) and (d).

As seen in figure 6(c) and (d) , the $\bar{2}\,\bar{2}\,0$ SXRT transmission section images show exactly the same black tail directions and lengths as predicted by the orientation contrast simulation for both ns (c) and fs (d) laser machining cases. Therefore, the [001] crystal plane bending directions as hypothesised in figure 3 are clearly proven by both large area back reflection and transmission section techniques. Although the

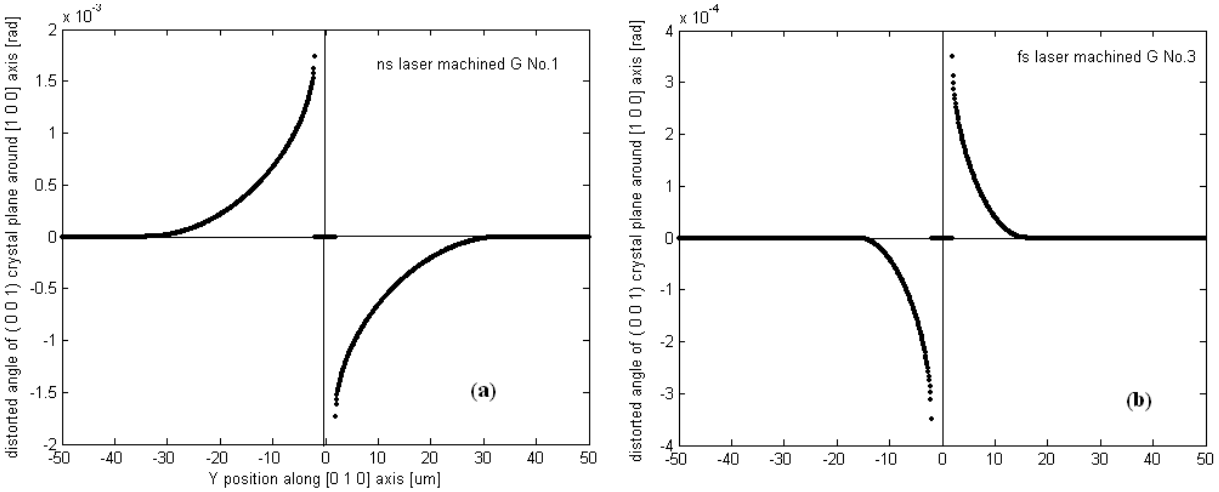


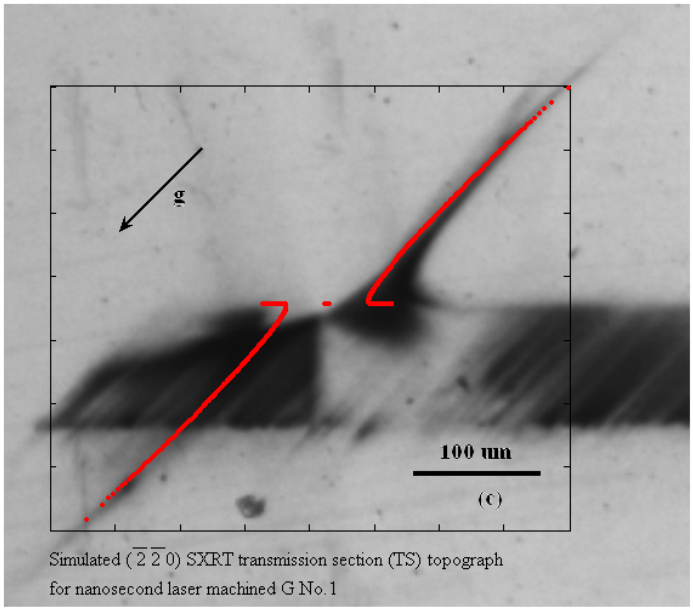


Simulated ( $\bar{2}\,\bar{2}\,0$) SXRT transmission section (TS) topograph for nanosecond laser machined G No.1

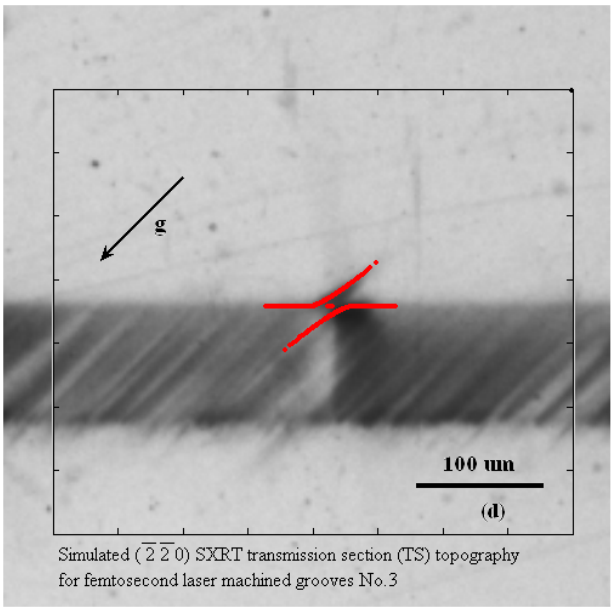


Simulated ( $\bar{2}\,\bar{2}\,0$) SXRT transmission section (TS) topography for femtosecond laser machined grooves No.3

real curve shape of the distorted [100] crystal plane may not be exactly the same as indicated by Equation (4) and (5), we can still conclude that, with our current laser machining parameters, femtosecond laser machining will compress the [001] crystal plane underneath while ns laser pulses will tilt the [001] crystal plane upwards and leave the same region in tension instead. In addition, the simulation shows a gradual reduction in intensity towards the end of the diffracted 'tails'. This is also seen on the experimental film confirming the increased misorientation as one approaches the groove centre. SXRT is proven to be a very sensitive tool for detecting crystal plane distortion after laser machining treatments. Both the magnitude and sign of the shear

strain can be calculated after careful modelling.

**Figure 6:** Synchrotron x-ray transmission section topograph simulation: the distorted angle of (001) crystal plane around [100] axis for (a) ns laser machined G No.1 and (b) fs laser machined G No.3; Positive values represent clockwise rotation along [100] axis. The simulated $\bar{2}\bar{2}0$ SXRT transmission section images: (c) for nanosecond laser machined G No.1 and (d) femtosecond laser machined G No.3 on the backgrounds of the experimental SXRT images.

### Micro-Raman Spectroscopy results

When compared to Synchrotron X-ray Topography (SXRT), micro Raman spectroscopy (uRS) has the capability to measure the localized strain distribution with better lateral resolution as determined by the laser spot size, which is 1 um in this study. Raman Spectroscopy has already been found to be sensitive to the presence of amorphous and polycrystalline InP and it is possible to analyse the strain distribution and polycrystalline grain size inside the re-crystallized layer on the top surface. [2] The probe depth of the Raman measurements can be calculated depending on the material and its crystalline state. Using the 488 nm $Ar^+$ laser output, the average optical penetration depth in single-crystalline indium phosphide (c-InP) is ~70 nm [19], which is far smaller than the minimum x-ray penetration depth even in the back reflection geometry (2.78 um). Therefore, combining SXRT and uRS techniques, a comprehensive strain profile from the top surface to the bottom surface induced by laser machined grooves can be non-destructively obtained.

As shown in figure 7, the reference spectrum of an untreated (100) InP sample, shown as the black curve is obtained far away from the laser machined grooves. Several first and second order Raman peaks are visible. The first longitudinal optical (LO) phonon-peak appears at approximately 339.5$cm^{-1}$ arising from the surface depletion zone. The small LO peak intensity suggests a high carrier concentration in the InP sample, which reduce the scattering volume for the unscreened LO mode and hence the depletion depth. Adjacent to three second-order phonon peaks (2TO: 614$cm^{-1}$, 2LO: 679$cm^{-1}$ and TO+LO: 648$cm^{-1}$), a broad feature assigned to one of the LO phonon-plasmon coupled modes (LOPCM: $L^+$) can be observed at ~594$cm^{-1}$. Since the peak position of the $L^+$ coupled mode has been found to be very sensitive to the free-carrier density in n-InP, a carrier concentration of about $3.5*10^{18}$ $cm^{-3}$ can be estimated by comparing to the data in the literature [18]. This is in agreement with the InP sample doping level indicated in section 3. At such high doping levels, the excited

carrier population induced by the incident laser can be neglected and thus the $L^+$ peak presents a very slight blue shift with decreasing exciting laser power used in the Raman measurements. According to the InP selection rule for the back-reflection geometry employed in this study, the transverse optical (TO) phonon-peak at ~306 $cm^{-1}$ should be forbidden and should show a very low intensity. The overlapping strong peak at ~301.4 $cm^{-1}$ is attributed to another LOPCM mode ($L^-$) instead. Similar Raman spectra can be found in the literature where the 528.7 nm line of an $Ar^+$ laser has been used as an exciting source for the Raman measurements on heavily doped n-InP [18].

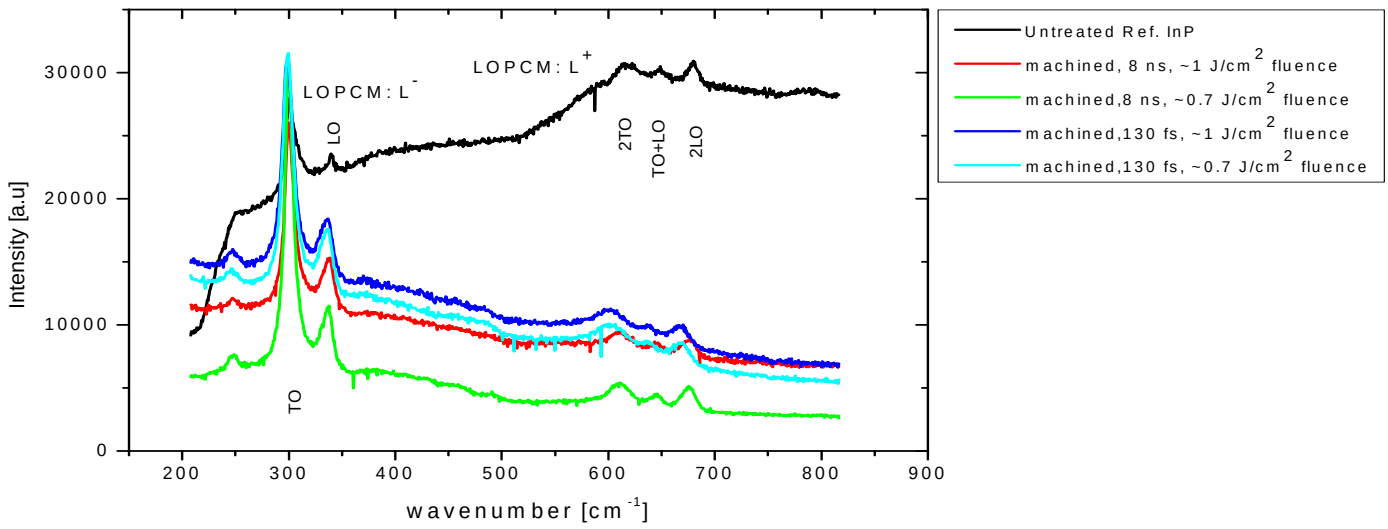


**Figure 7:** Typical Raman Spectrum on untreated InP (100) crystal and the surface at the centre of four different laser machined grooves.

In contrast, for all the Raman spectra measured inside the grooves, no LOPCM:$L^+$ mode can been seen at the high frequency range (500 $cm^{-1}$ ~ 800 $cm^{-1}$), which suggests a greatly reduced free carrier concentration on the laser machined surface. Therefore, no $L^-$ peak can been expected at the overlapping peak position of the TO mode. The two strong Raman peaks observed at approx 300 $cm^{-1}$ and 338 $cm^{-1}$ are now related to TO and LO modes, respectively, excited from the top surface re-crystallized layer. The presence of the TO mode arises from the less than ideal backscattering geometry due to the presence of poly-crystalline InP and light scattering from the rough laser machined surface. Compared to the dominant TO and LO peaks, the broad disorder activated optical phonon mode (DAO) peak, which can be related to the InP amorphous layer, are not obvious at ~ 300 $cm^{-1}$ and ~ 440 $cm^{-1}$

[2]. This phenomenon indicates that, for all the fs or ns laser machined grooves, the amorphous layer thickness is far smaller than that of the polycrystalline InP through to the 70 nm Raman probe depth. From the coexistence of LO and TO phonon peaks and the missing LOPCM mode for all the Raman spectra obtained inside the machined areas, it appears that all the laser machined grooves investigated in this paper are covered by a thick re-crystallized poly-crystalline layer. The layer thickness should exceed 70 nm (the Raman excitation laser penetration depth), which is consistent with the XTEM results on those samples [6]. The increased disorder of the crystallite orientation in this re-solidified layer is further supported by the fact that the full width at half maximum (FWHM) of the LO peak increases by a factor of 3 to 4 compared to the regions outside laser machined grooves.

For InP, Raman spectroscopy is also very useful for direct mechanical stress calculations. Assuming uniaxial stress, the internal stress $\delta$ is linearly related to the shift of Raman peak $D\omega$ (compared with its peak position of unstressed the surface):

$$\delta = gD\omega \qquad (12)$$

where a negative value of $\delta$ indicates compressive stress in the tested material and $g$ has a value of –0.19GPa/cm$^{-1}$ for the InP LO-phonon mode[20]. Therefore, a positive shift in the InP LO peak reveals a compressive stress. Since the Raman signal inside the grooves is mainly derived from a poly-crystalline layer, it is very important to notice that the shift to lower wavenumber for the InP LO phonon peak could also be introduced by the decreased crystallite size due to the quantum confinement effect [21]. The measured Raman peak shift must be calibrated before the stress calculation.

As shown in figure 8, which shows the FWHM line profile of the LO peak across four laser machined grooves, the LO peaks broaden to 19 cm$^{-1}$ for nanosecond laser machining and have an average value of 12 to 14 cm$^{-1}$ in all irradiated areas. According to the calculation of Yu et al. using the spatial correlation mode for InP along the [100] direction, the InP LO peak broadens with decreasing mean diameter of the InP crystallite size. [22] The FWHM values of 12 and 14 cm$^{-1}$ are correlated to a lateral crystallite dimension of 4.1 nm and 3.8 nm, respectively, which will cause a downward shift of the LO peak by about -1 cm$^{-1}$. By assuming that the polycrystalline InP has a characteristic LO peak FWHM value of more than 11 cm$^{-1}$, the re-crystallized layer widths on the top surface across the four laser machined grooves from No.1 to No.4 have been measured to be 14.82 μm, 9 μm, 20 μm and 10 μm, respectively. They are much smaller than the subsurface strained crystal width measured by the SXRT methods. The big variation of the LO peak FWHM outside the grooved area (at the scan position from 45 μm to 57 μm) in figure 8 (a) is correlated with the presence of droplet particles deposited by a liquid phase expulsion process

observed on the XTEM images [6].

With our current experimental configuration, the width of the re-crystallized layer appears to increase with decreasing pulse duration and increasing pulse energy. According to the XTEM results, the groove surface, machined by both fs and ns laser pulses are fully covered by a ~ 300 nm thick poly-InP layer. [5] The re-crystallized layer width measured by the Raman method is equal to the laser machined groove width. The groove width increase with shorter laser pulse can be explained by enhanced optical energy absorption and reduced ablation threshold fluence, when the non-linear optical process becomes significant with the relatively higher peak intensities, achieved within fs pulse durations with the same pulse energies. [23]

When using the femtosecond laser machining method, the optical energy input occurs in ~ 130 fs, the resultant ultra fast phase transition (non-thermal melting) can be observed within ~ 400 fs, the onset of ablation occurs after ~ 200 ps and the resolidification time for InP is around 25 ns [23]. Compared to the nanosecond laser machining process, the energy deposition within a fs pulse duration is temporally separated from the consequent material removal process and there is no interaction of radiation with the ejected material. Therefore, a smoother groove surface and smaller Raman peak FWHM variation across the laser machined grooves can be expected. This is in agreement with uRs data, as shown in Figure 8.

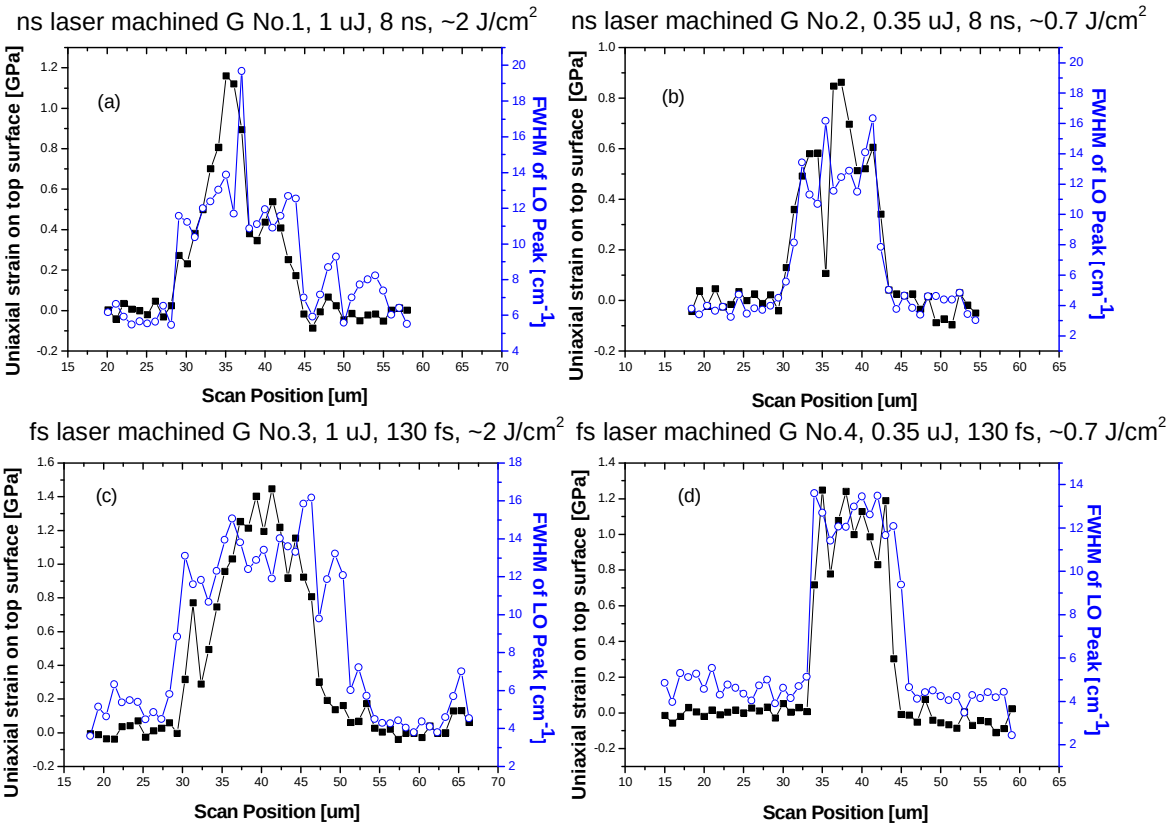


**Figure 8:** The line profile of calculated uniaxial strain on the top surface and full width at half maximum (FWHM) of LO phonon peak (open circles) across four laser machined grooves with: (a) ~1 J/cm$^2$ laser peak fluence, 8 ns pulse duration, (b) ~0.7 J/cm$^2$ laser peak fluence, 8 ns pulse duration, (c) ~1 J/cm$^2$ laser peak fluence, 130 fs pulse duration and (d) ~0.7 J/cm$^2$ laser peak fluence, 130 fs pulse duration. The LO peak positions and FWHM at each scan position has been measured in each Raman spectrum using multi-peaks fitting with OriginPro 7.5® software.

After calibrating the InP LO peak position with the corresponding FWHM value using Yu's model [22], the line profile of uniaxial stress on the top surface (~ 70 nm probing depth) across the four laser machined grooves has been calculated as shown in figure 8. Only tensile stress has been found in the poly-crystalline layer on the top surface and the maximum values for grooves from No.1 to No.4 are estimated to be 1.16 GPa, 0.863 GPa, 1.45 GPa and 1.24 GPa, respectively. This surface tensile strain can arise either from thermocapillary or from chemicapillary effects. The thermocapillary force, induced by the temperature gradient due to the Gaussian beam profile, moves the materials to the cooler (outer) region. The chemicapillary force causes the mass diffusion of phosphorous due to a concentration gradient induced by the depletion of

phosphorous at the free surface. [24] The maximum tensile stress found at the center of our fs laser machined grooves (2 J/cm$^2$, 130 fs) is about 4 times higher than the stress value of + 0.32 GPa reported by J. Bonse et al. (1.8 J/cm$^2$, 130 fs) [2]. The different stress values most likely arise from the different laser machining process consisting of multiple laser pulse irradiation. While cutting grooves on InP wafer surface, the same laser spot position has been irradiated by ~ 10 pulses in this study, rather than a single or double pulse in [2].

The uniaxial strain values estimated from Raman measurements are much higher than the shear strain induced by crystal plane distortion estimated by the SXRT images. It should be noted that the SXRT information is from the InP crystal to the depths of many tens of micrometers underneath rather than from the the poly-InP layer within a 70 nm depth from the surface measured by Raman spectroscopy.

Inside the laser machined grooves, the average tensile stress is higher with femtosecond laser pulse durations and higher laser pulse energies. The uniformity of uniaxial strain distribution inside the grooved area has been found to be improved by femtosecond laser machining methods.

| Groove: | No.1 | No.2 | No.3 | No.4 |
|---|---|---|---|---|
| Pulse Duration | 8 ns | 8 ns | 130 fs | 130 fs |
| Pulse Energy (μJ) | 1 | 0.35 | 1 | 0.35 |
| Laser peak fluences (J/cm$^2$) | ~2 | ~0.7 | ~2 | ~0.7 |
| Maximum rotated angle of crystal plane $(\bar{2}\,\bar{2}\,0)$ around [100] (mrad) | 1.74 | 0.54 | 0.35 | 0.24 |
| Width of poly-crystallized InP layer on top surface across the grooves (μm) | 14.82 | 9 | 20 | 10 |
| Width of distorted crystal region underneath surface across the grooves (μm) | 64 | 32 | 28 | 24 |
| Depth of shear strained crystal region (μm) | >20 | >20 | -- | -- |
| Shear stress magnitude of distorted InP crystal about the grooves (MPa) | 106.2 | 33.4 | 22.2 | 14.1 |
| Tensile stress magnitude in poly-crystalline InP layer on top (GPa) | 1.16 | 0.863 | 1.45 | 1.24 |

**Table 1:** The SXRT and micro-Raman results summary for the four laser machined grooves

## 5. Conclusion:

We have studied a set of femtosecond and nanosecond laser machined grooves on one (001) InP substrate using synchrotron x-ray topography (SXRT) and micro-Raman Spectroscopy (μRS). A three-dimensioned map of strain about the grooves running from the recrystallized poly-crystalline layer on the top surface through to the distorted crystal substrate hundreds of micrometers deep underneath has been analyzed non-destructively.

With our current laser machining parameter setup, femtosecond laser machining has been found to compress the (001) crystal plane about the grooves while ns laser pulses tilted the (001) crystal plane towards the surface and left the same area in tension instead. The reversed sign of shear strain distribution on both sides of laser machined grooves using ns and fs laser pulse can be concluded using SXRT method, which is in good agreement with the measurement results of the rotated degree of polarization (ROP) photoluminescence (PL) technique, a destructive tool used in strain analysis for direct band-gap semiconductors. [5]

For both femtosecond and nanosecond cases, the tensile stress on the top surface was much bigger than the shear stress magnitude in the subsurface distorted crystal and was localized in a much smaller volume, a thin layer of resolidified poly-InP on the groove surface.

The magnitude of crystal plane distortion and the width of the shear strained regions tens of micrometers below the femtosecond laser machined grooves was smaller than the nanosecond counterparts with the same pulse energy. The uniformity of uniaxial tensile stress distribution on the groove surface was improved when using femtosecond laser pulse, which can be related to the less interaction between laser and ablated materials. However, according to the micro-Raman results, the average tensile stress on the machined groove surface was slightly higher for femtosecond laser pulse durations and higher laser pulse energies.

## 6. Acknowledgements

The authors would like to acknowledge the financial support from Enterprise Ireland Commercialization Fund Technology Development (CFTD) Scheme. The synchrotron x-ray topograph experiment was supported by the European Community Research Infrastructure Action under the FP6 "Structuring the European Research Area" Programme (through the Integrated Infrastructure Initiative "Integrating Activity on Synchrotron and Free Electron Laser Science") with contract RII3-CT-2004-506008. The support of C. Paulmann and T. Wroblewski at HASYLAB Beamline F-1 is gratefully acknowledged.

## 7. References:


[1] Ajay Malshe and Devesh Deshpande 2004 *Journal of Materials Processing Technology* **149** 585

[2] J. Bonse, JM. Wrobel, K.-W. Brzezinka, N. Esser, W. Kautek, 2002, *Applied Surface Science* **202** 272

[3] M.S. Amer, M.A. El-Ashry, L.R. Dosser, K.E. Hix, J.F. Maguire and Bryan Irwin 2005 *Applied Surface Science* **242** 162

[4] J. Bonse, JM. Wrobel, J. Krüger, W. Kautek, 2001 *Applied Physics A* **72** 89

[5] A. Borowiec, D. M. Bruce, D. T. Cassidy, H. K. Haugen 2003 *Applied Physics Letter* **83** 225

[6] A. Borowiec, M. Couillard, G. A. Botton, H. K. Haugen, 2004 *Applied Physics A: Material Science & Processing* **79** 1887

[7] Y. Jee, M.F. Becker, R.M. Walser, 1988 *J. Opt. Soc. Am. B* **5** 648

[8] D. K. Bowen and B. K. Tanner, 1998 *High resolution X ray Diffractometry and Topography* London, U.K.: Taylor & Francis

[9] Patrick J. McNally, R. Rantanmaki, T. Tuomi, A. N. Danilewsky, Donnacha Lowney, John W. Curley and P. A. E. (Toney) Herbert, 2001, *IEEE Transactions of Components and Packaging Technology* **24** 76

[10] J. Kanatharana , J.J. Pėrez-Camacho , T. Buckley , P.J. McNally, T. Tuomi, A.N. Danilewsky, M. O'Hare , D. Lowney , W. Chen , R. Rantamaki, L. Knuuttila, J. Riikonen 2003 *Microelectronic Engineering* **65** 209

[11] A. Lankinen, L. Knuuttila, T. Tuomi, P. Kostamo, A. Säynätjoki, J. Riikonen, H. Lipsanen, P.J. McNally, X. Lu, H. Sipilä 2006. *Nuclear Instruments and Methods in Physics Research Section A: Accelerators, Spectrometers, Detectors and Associated Equipment* **563** 62

[12] G. D. Yao, M. Dudley, J. Wu, 1990 *Journal of X-Ray Science and Technology* **2** 195

[13] M Dudley, X R Huang and W Huang, 1999 Journal of Physics D: Applied Physics **32** A139

[14] A. Authier, S. Lagomarsino, B.K. Tanner (Eds.), 1996 *X-ray and Neutron Dynamical Diffraction: Theory and Applications*, Plenum Press, New York

[15] J. Kanatharana , J.J. Pėrez-Camacho , T. Buckley , P.J. McNally, T. Tuomi, A.N. Danilewsky, M. O'Hare , D. Lowney , W. Chen , R. Rantamaki, L. Knuuttila, J. Riikonen 2003 *Journal of Physics D: Applied Physics* **36** A60

[16] http://www.ioffe.rssi.ru/SVA/NSM/Semicond/InP/mechanic.html

[17] R. Rantamäki, T. Tuomi, Z. R. Zytkiewicz, J. Domagala, P. J. McNally and A. N.

Danilewsky, 1999 *Journal of Applied Physics* **86** 4298

[18] L. Artùs, R. Cuscò, J. Ibàñez, N. Blanco and G. Gonzàlez-Diaz, 1999 *Physical Review B* **60** 5456

[19] Aspnes, D. E. and A. A. Studna, 1983 *Physics Review B* **27** 985

[20] R. Trommer, H. Müller, M. Cardona and P. Vogl, 1980, *Physics Review B* **21** 4869

[21] J. H. Campbell and P. M. Fauchet, 1986 *Solid State Communications* **58** 739

[22] S.J.Yu, H.Asahi, S.Emura, H. Sumida, S. Gonda and H. Tanoue, 1989 *Journal of Applied Physics* **66** 856

[23] J. Bonse, S.M. Wiggins and J. Solis, 2005 *Applied Physics: A* **80** 243.

[24] T. D. Bennett, D. J. Krajnovich, C. P. Grigoropoulos, P. Baumgart, A. C. Tan, *J. Heat Trans.* – T. ASME 119 (1997) 589.